According to these results, the optimal high resolution diffraction limit was determined as 1.80Å resolution. It does not look like a large difference in comparison with the previous choice (1.85 Å). However, the resolution shell 1.85–1.80 Å contains 9,929 unique reflections (8 % of whole dataset) which is not a negligible number, given the number of refined parameters (45,388).

1. P. A. Karplus & K. Diederichs, *Science* **336**, (2012), pp. 1030–1033.

2. W. Kabsch, *Acta Cryst. D*, **66**, (2010), 125.

3. G. N. Murshudov, A. A. Vagin, E. J. Dodson, *Acta Cryst. D*, **53**, (1997), pp. 240–255.

4. M. Stranava *et al.*, *J. Biol. Chem.*, **292**, (2017), pp. 20921-20935.

Session II

SL7

STUDY OF THE REAL STRUCTURE OF THE LASER-CLADDED STEEL

Karel Trojan[1], Václav Ocelík[2], Jiří Čapek[1] and Nikolaj Ganev[1]

[1]*Department of Solid State Engineering, Faculty of Nuclear Sciences and Physical Engineering, CTU in Prague, Trojanova 13, 120 00 Prague 2, Czech Republic*
[2]*Department of Applied Physics, Zernike Institute for Advanced Materials, Faculty of Science and Engineering, University of Groningen, Nijenborgh 4, 9747 AG, Groningen, The Netherlands*

AISI H13 hot working tool steel is one of the most common die material used in metal and casting industries. Dies suffer damage due to wear and thermo-dynamic stresses during their lifetime [1]. Therefore, various methods have been developed for their repair, which is cheaper than manufacturing new ones. A great benefit of laser cladding in this field is a high productivity with minimal influence due to a low heat input on surrounding material by thermal stresses [2]. Therefore, the aim of the contribution is to describe the effects of laser processing on the microstructure of laser cladded H13 tool steel using orientation imaging microscopy (OIM) based on electron backscatter diffraction (EBSD) and other techniques.

Laser cladding was carried using an IPG 3 kW Yt:YAG fibre laser. The laser power density of 114 J/mm^2 was applied to form a volume consisting of five overlapping layers, see Fig. 1. The martensitic structure was observed on the cross-section of the clad using electron backscattering diffraction, see inverse pole figures (IPF) of ferritic phase in Fig. 2. The original austenite grains with a characteristic size of 20–50 µm, which were formed during the transition of the melt into a solid phase and whose were subsequently transformed into martensitic or bainitic laths, are clearly seen in the figure. It has to be noted that the EBSD technique is not able directly distinguish ferrite and martensite.

Further, the clads were subjected to X-ray diffraction measurement, tensile testing, wear resistance and hardness measurement for comprehensive utilization evaluation of laser cladding.
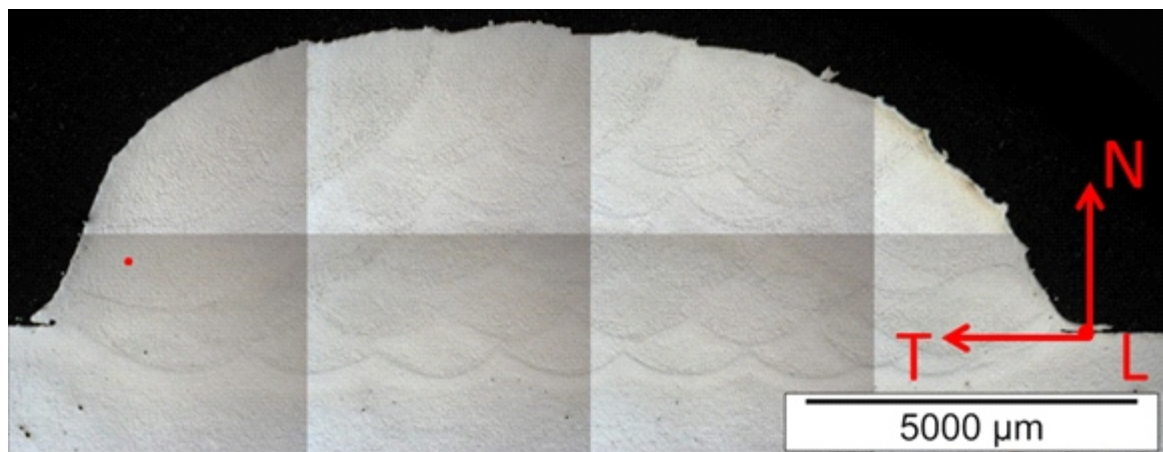
Figure 1: Metallographic cross-section of the clad AISI H13 tool steel with marked directions and area which was observed using OIM.
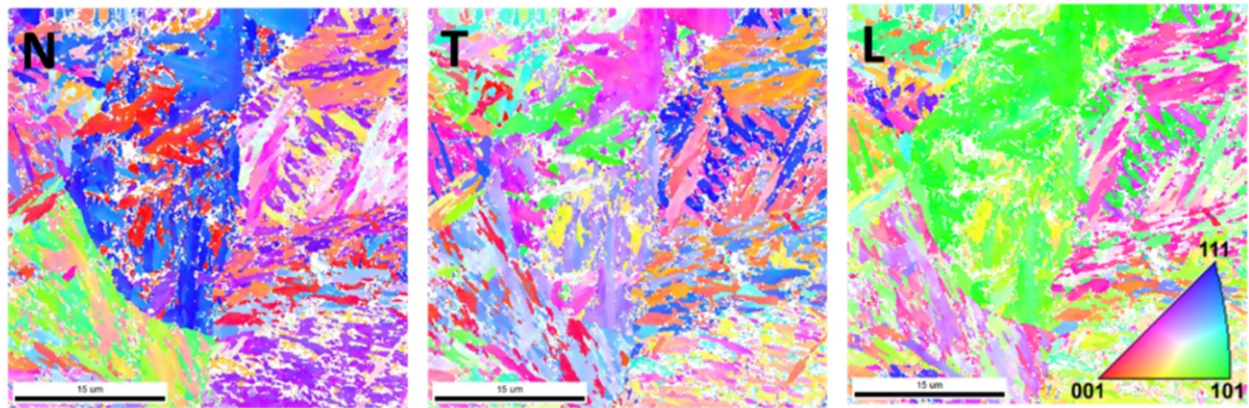
Figure 2: IPF maps of ferritic phase for different directions in the selected area, where N, T, and L denote the directions.

1. G. Telasang, J. Majumdar, N. Wasekar, G. Padmanabham, I. Manna, Microstructure and Mechanical Properties of Laser Clad and Post-cladding Tempered AISI H13 Tool Steel. Metall. Mater. Trans. A. 46A (2015) 2309-2321.

2. M. Vedani, B. Previtali, G.M. Vimercati, A. Sanvito, G. Somaschini, Problems in laser repair-welding a surface-treated tool steel, Surf. Coat. Tech. 201 (2007) 4518-4525.

SL8

THERMALLY INDUCED CHANGES IN MODULATED STRUCTURE OF 10M Ni$_{50}$Mn$_{27}$Ga$_{22}$Fe$_1$ MARTENSITE

P. Veřtát[1,2], L. Straka[2,3], O. Pacherová[2], M. Klicpera[3], A. Sozinov[4], O. Heczko[2]

[1]Faculty of Nuclear Sciences and Physical Engineering, Czech Technical University in Prague, Prague, 11519, Czech Republic
[2]Institute of Physics, Czech Academy of Sciences, Prague, 18221, Czech Republic
[3]Faculty of Mathematics and Physics, Charles University, Prague 2, 12116, Czech Republic
[4]Material Physics Laboratory, LUT University, Lappeenranta, 53850, Finland
vertat@fzu.cz

The observation of magnetic shape memory (MSM) effect in Heusler alloy Ni$_2$MnGa by Kari Ullakko [1] stimulated tremendous scientific interest in this class of materials. The MSM alloys possess many practical applications in sensors [2], actuators [3, 4], micropumps [5] and energy-conversion devices [6]. From the fundamental point of view, the MSM effect includes the magnetically induced thermoelastic martensitic transformation and magnetically induced structural reorientation of martensite, where the extremely mobile twin boundaries of martensite play and essential role.

The structure of martensite of the Ni-Mn-Ga-based alloys is often modulated, depending on composition and temperature. Although the modulated structure is decisive in the aforementioned extremely mobile twin boundaries of Ni-Mn-Ga alloys, the character of modulation is still under discussion – especially for the 10M modulated martensite, for which the highest twin boundary mobility is found. For different compositions, the "10M martensite" was reported to have commensurate or incommensurate modulation [7-10] or to be nanotwinned [11, 12]. Both incommensurate and nanotwinned structure can result in similar apparent changes in modulation vector. Considering the incommensurality approach, it has been shown that the modulation vector changes gradually with temperature [7, 9].

Using neutron and X-ray diffraction on single crystal of Ni$_{50}$Mn$_{27}$Ga$_{22}$Fe$_1$ alloy, we discovered transition between commensurate and incommensurate modulated structure with changing temperature (Fig. 1) and followed its evolution in 10M martensite. We observed that doping of the Ni-Mn-Ga alloy with Fe leads to accentuation of the modulation satellites and it also leads to shifting of the temperature ranges of occurrence of different martensites, which is likely favourable for the applications.

We found that the discovered transition exhibits thermal hysteresis around the room temperature. Owing to the hysteresis, sample can be prepared in commensurate or incommensurate state at the same temperature using appropriate heating/cooling procedure. Observed transition was confirmed by resistivity measurements and by scanning electron microscopy. The investigation whether the incommensurality is proper or only apparent caused by nanotwinning is the subject of ongoing research.

1. K. Ullakko, J. K. Huang, C. Kantner, R. C. O'Handley, V. V. Kokorin, *Applied Physics Letters*, **69**, (1996), 1966.

2. J. M. Stephan, E. Pagounis, M. Laufenberg, O. Paul, P. Ruther, *IEEE Sensors Journal*, **11**, (2011), 2683.

3. R. C. O'Handley, K. Ullakko, *High-strain, magnetic field-controlled actuator materials, US patenUS5958154A,* 1997.
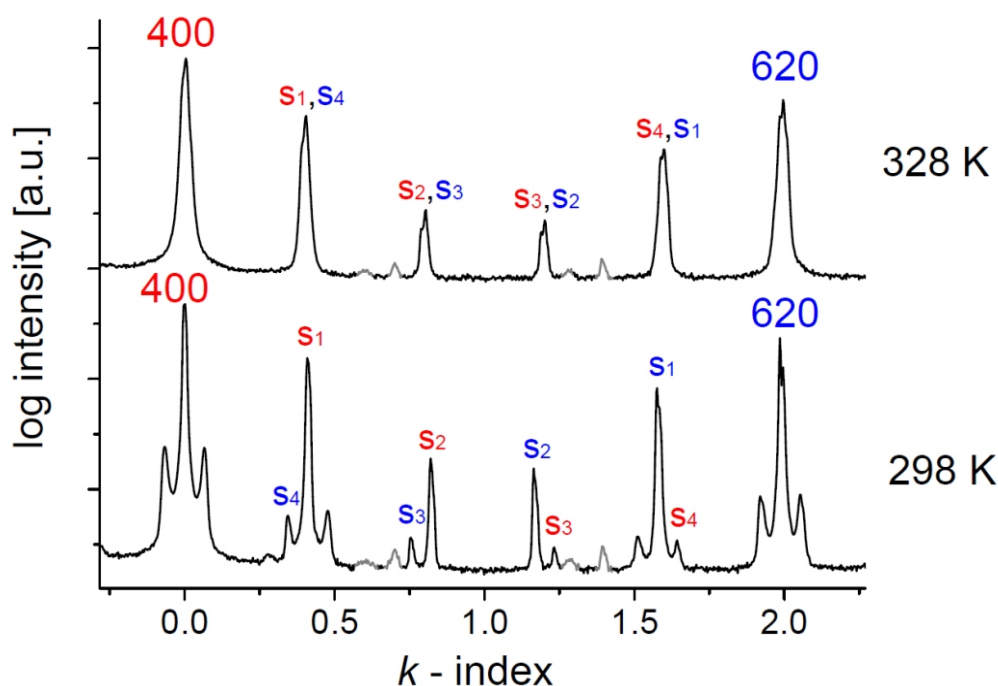
Figure 1. Measured q-scans in the [110] direction of the reciprocal space. At 298 K, the measurement indicates in-commensurate 10M modulated martensite. Upon heating to 328 K, the structure transforms to commensurate 10M. Modulation satellites belonging to 400 and 620 reflections are marked red and blue. The slight splitting of the peaks is caused by the mosaicity of the crystal and a/b twinning. Reflections from the sample holder are marked grey.

4. J. Tellinen, I. Suorsa, A. Jääskeläinen, I. Aaltio, K. Ullakko, in *Proceedings of the 7th International Conference on New Actuators, Actuator 2002, Bremen, Germany*, edited by H. Borgmann, 2002, pp. 566-569.

5. A. R. Smith, D. Fologea, P. Müllner, in *Proceedings of the 18th International Conference on New Actuators, Actuator 2008, Bremen, Germany*, edited by H. Borgmann, 2018.

6. N. M. Bruno, C. Ciocanel, H. P. Feigenbaum, A. Waldauer, *Smart Materials and Structures*, **21**, (2012), 094018.

7. L. Righi, F. Albertini, A. Paoluzi, S. Fabbrici, E. Villa, G. Calestani, S. Besseghini, *Materials Science Forum*, **635**, (2010), 33.

8. T. Fukuda, H. Kushida, M. Todai, T. Kakeshita, H. Mori, *Scripta Materialia,* **61**, (2009), 473.

9. A. Çakir, M. Acet, L. Righi, F. Albertini, M. Farle, *AIP Advances*, **5**, (2015), 097222.

10. S. O. Mariager, T. Huber, G. Ingold, *Acta Materialia*, **66**, (2014), 192.

11. S. Kaufman, U. K. Rößler, O. Heczko, M. Wuttig, J. Buschbeck, L. Schultz, S. Fähler, *Physical Review Letters*, **104**, (2010), 1457029.

12. L. Straka, J. Drahokoupil, P. Veřtát, M. Zelený, J. Kopeček, A. Sozinov, O. Heczko, *Scientific Reports*, **8** (2018), 11943.

COMPARISON OF THE ROLLING TEXTURE OF PARTICULAR PHASES OF DUAL-PHASE STEEL WITH SINGLE-PHASE STEELS

J. Čapek, K. Trojan, N. Ganev

Department of Solid State Engineering, Faculty of Nuclear Sciences and Physical Engineering,
Czech Technical University in Prague
jiri.capek@fjfi.cvut.cz

Duplex steels are dual-phase steels with 50/50 proportion of ferrite (-Fe) and austenite (-Fe) phases. Because of the combination of properties of both the phases in dual-phase microstructure, duplex steels are distinguished by good properties in many environments, where the standard austenitic and ferritic steels are usually used [1]. Due to very often presence of preferred orientation (texture) in these materials, analysis and consequent interpretation of the texture is crucial, especially in material engineering. The importance of study the texture resides in the anisotropy of most material properties induced by its presence. Because of different mechanical properties of ferrite and austenite phases, their behaviour during deformation, generally spoken, is different in dual-phase steel in comparison with single-phase steels [2].

The plate shape samples of size 19×120 mm^2 and different thicknesses were made of AISI 420 (ferritic), AISI 304 (austenitic) and AISI 318LN (duplex) type of stainless steels. The samples were cold-rolled with 0, 10, 20, 30, 40, and 50% reduction of thickness, so the final thickness of all samples was 1.5 mm. Samples made of ferritic, austenitic and duplex steel were marked as F0–F50, A0–A50 and D0–D50, respectively.

The *X'Pert PRO MPD* diffractometer with cobalt radiation was used to the RD-TD plane samples analyses by X-ray diffraction, where rolling (RD), transversal (TD) and normal (ND) directions create a coordination system of the sample. Texture analysis was performed based on orientation distribution function (ODF) calculated from experimental pole figures obtained by analysis of three diffraction lines {110}/{220}, {200}, {211} of ferrite phase and {111}/{311}, {200}, {220} of austenite phases.

The rolling texture of ferrite may be described by several texture fibres [3], for example, the limited   and , see Fig. 1. Ferritic steel exhibits the typical texture components: {001}n, {112}n, and {111}n. For austenitic steel, the rolling texture is usually composed of , , and   texture fibres. The typical texture components of these materials are Brass, Goss, and Copper [3]. Nevertheless, it is necessary to expect that dual-phase steel should have different behaviour of the constituent phases in comparison with single-phase steel. It has been found that ODFs of ferrite phase of the duplex steel do not consist of texture fibres, but only of the particular texture components. For austenite phase of the duplex steel, fewer texture components and fibres are generated compared to the austenitic steel.

The presence of two phases results in a decrease of strain hardening speed. The reason for that behaviour is the partition of plastic deformation occurring within both the phases, during cold rolling. The strain hardening of austenite is very high at low deformations, but at about 15%

Sample F50

Sample D50 -   phase

Sample A50

Sample D50 -   phase
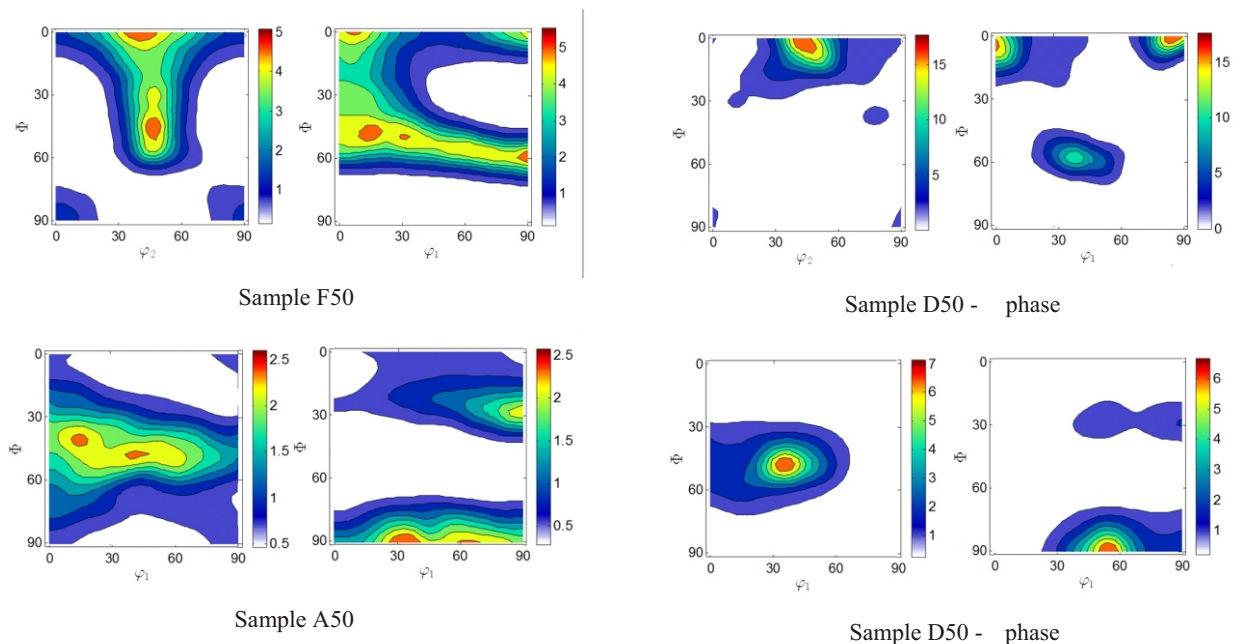
Figure 1. Selected orientation distribution functions in the $_1 = 0°$ (left) and $_1 = 45°$ (right) sections for   phases, and $_2 = 0°$ (left) and $_2 = 45°$ (right) sections for   phases.

thickness reduction it gets increasingly concentrated within the ferrite phase, which has a larger number of active slip systems and a considerably higher stacking-fault energy [4]. Therefore, the typical texture fibres of the phases in the dual-phase steel are not generated but only strong separated texture components are presented. However, the typical texture component and fibres are generated in the sample with higher deformation.

1.   R. Dakhlaoui, C. Braham, A. Baczmański, *Mater. Sci. Eng.: A.*, **444**, (2007), 6-17.

2.   J. Ryś, W. Ratuszek, M. Witkowska, *Arch. Metall. Mater.*, **51**, (2006), 495-502.

3.   H. J. Bunge, *Texture Analysis in Materials Science*. London: Butterworth. 1982.

4.   I. Alvarez-Armas, S. Degallaix-Moreuil, *Duplex stainless steels*. John Wiley & Sons. 2013.

SL10

CRYSTAL STRUCTURE AND PROPERTIES OF SrTi₁₋ₓMnₓO₃ PEROVSKITES – FROM CALCULATIONS TO EXPERIMENTS

M. Lebeda[1], J. Drahokoupil[2]

[1]Faculty of Nuclear Sciences and Physical Engineering, Czech Technical University in Prague, Prague, Czech Republic
[2]Institute of Physics of the Czech Academy of Sciences, Prague, Czech Republic
leb.miroa@seznam.cz

The $SrTi_{1-x}Mn_xO_3$ ceramics were experimentally studied by X-ray diffraction and resonant ultrasound spectroscopy and the results were compared with the theoretical calculation from DFT. Firstly, it was confirmed that our samples were crystallized as cubic and the dependence of lattice parameter a on Mn concentration was determined. The linear decrease of a with increasing Mn can be seen in Fig. 1 - left. Therefore, it can be expected that it follows Vegard's law. Subsequently the comparison between those lattice parameters obtained by X-ray diffraction measurements and the values calculated by DFT method in CASTEP module of Materials Studio was performed.

Secondly, the calculation of the free energy of $SrTi_{1-x}Mn_xO_3$ as a function of the volume of the unit cell was calculated from the first-principles and the obtained dependence was fitted by Birch-Murnaghan equation of state [1], which allowed the estimation of the bulk modulus and equilibrium volume of the unit cell. Furthermore, the change of the calculated bulk modulus caused by the differ-

ent fitted volume range was tested and the resulting dependence is emphasized for the pure $SrTiO_3$ in Fig.1 – right, with the experimental value [2]. The calculated data are in very good agreement with the corresponding experiment: in all studied perovskites the relative deviations from the experimental values are in the case of the lattice parameter only up to two percent and in the case of the bulk modulus up to four percent.

1.   F. Birch. Finite elastic strain of cubic crystals. Phys. Rev. 71(11): 809, 1947.

2.   R. O. Belt, G. Rupprecht. Elastic constants of strontium titanite. *Phys. Rev.* 129(1): 90, 1963.
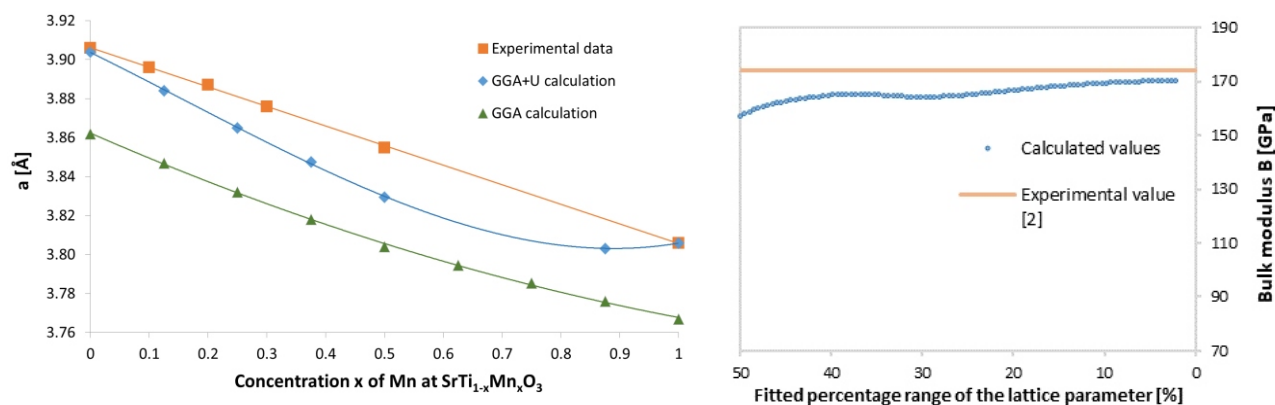
Figure 1. **Left:** experimentally observed linear decrease of the lattice parameter a with increasing Mn concentration at $SrTi_{1-x}Mn_xO_3$ cubical perovskites (squares) and the lattice parameters data from ab-initio simulations with GGA, resp. GGA+U functional (triangles, resp. rhombuses). **Right:** dependence of the $SrTiO_3$ bulk modulus on the different fitted percentage range of the volume (lattice parameter) of the unit cell at Birch-Murnaghan equation of state. The straight line indicates the experimental value [2].

SL11

STRUCTURAL ANALYSIS OF PEROVSKITE THIN FILMS AND MULTILAYERS

T. Číž, M. Kiaba, O. Caha, A. Dubroka

Department of Condensed Matter Physics, Faculty of Science, Masaryk University, Kotlářská 2, 61137 Brno, Czech Republic
444338@mail.muni.cz, caha@physics.muni.cz

Perovskite oxides with chemical formula ABO_3 have many unique applications in modern matter science such as superconductivity, magnetoresistance or ferroelectricity. Compounds studied in this research are $LaFeO_3/SrTiO_3$ (LFO/STO). LFO is an insulator and in bulk form has no macroscopic magnetoelectric coupling or control of magnetism by electric field. In combination with semiconducting STO is created polar-nonpolar interface which makes it possible to achieve the above mentioned properties [1, 2].

The aim of this research is measuring the thickness of thin layers, roughness of interfaces and density of these compounds with method X-ray structural analysis, namely x-ray reflectivity and coplanar diffraction were used. The samples were prepared using pulsed laser deposition (PLD) technique in oxygen atmosphere at high temperature of approximately 700 °C and using compound polycrystalline targets.

The layer thickness t can be determined from the angular position of the daughter's maximum on the reflection curve. These maxima are caused by the interference of waves reflected from the upper and lower layers. The roughness of the interface   is largely influenced by the slope of the reflection curve. The density   is determined by the critical angle $_c$ [3].

The goal of the experiment is to measure the reflected intensity of the X-ray beam in dependence on the reflection angle   and its comparison with numerical simulation. This simulation allows to obtain all mentioned parameters of sample. In Fig. 1 is reflection curve, where is easy to recognise equidistant thickness oscillations. We have determined the thickness of the film as 11 nm and roughness of 0.6 nm.

Another part of this research is observation of reflected X-ray radiation from multilayers STO/LFO/STO. Here are discussed two different approaches. First of them is considering of each single atomic plane in stack. These samples were prepared using pulsed laser deposition (PLD) method by first depositing several atomic planes of the same material on top of each other, and subsequently applying the atomic planes of the other compound (complex model in Fig. 2). This process was subsequently repeated. The second approach neglect this manufacturing process and consider only one layer of each material with appropriate repetition. In Fig. 2 is superlattice with (3+3) x 4 monolayers. The data were fitted within the second approach with a model of 4 periods, each consisting of STO layer with thickness of 1.2 nm and LFO layer with thickness of 0.37 nm. The roughness of interface comes out as 0.46 nm for STO layer and 0.03 for LFO layer. If we sum the layer thickness of the individual layers in the complex model, we get similar results.
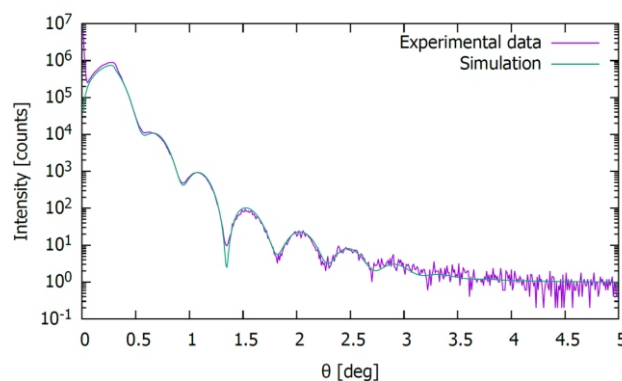
Figure 1. Example of measured reflectivity curve fitted by the simulation. The thickness can be determined from the frequency of the oscillations. This sample is a single layer of $LaFeO_3/SrTiO_3$ with thickness of 11 nm.
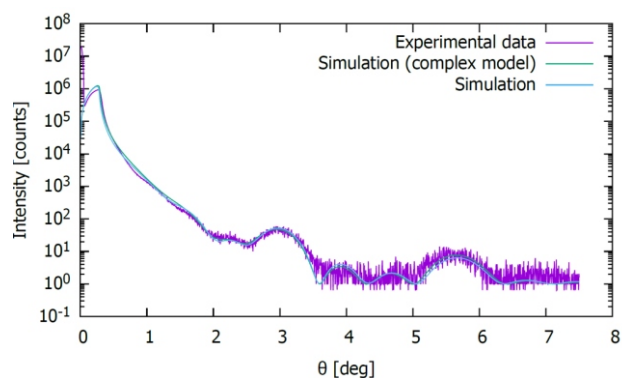
Figure 2. Reflection curve of superlattice STO/LFO/STO with (3+3) x 4 monolayers with two different simulations. In this case occurs extinction of maxima.

A total of about 12 samples with different thicknesses and number of periods were measured. All parameters were also determined for all. Finally, we have used method called reciprocal space mapping (RSM). This measurement has confirmed that all these samples are pseudomorphic.

1. LI, Lili, Guangbiao ZHANG, Jingyu LI, Dong CHEN, Zhenxiang CHENG a Yuanxu WANG. Electric field induced two-dimensional electron gas and magnetism in LaFeO3/SrTiO3 (0 0 1) heterostructures. *Applied Surface Science* [online]. 2019, **2019**(471), 185 - 195 [cit. 2019-05-01]. ISSN 0169-4332. Dostupné z: http://www.sciencedirect.com/science/article/pii/S0169433218333063

2. NAKAMURA, Kentarou, Hisanori MASHIKO, Kohei YOSHIMATSU a Akira OHTOMO. Impact of built-in potential across LaFeO3/SrTiO3 heterojunctions on photocatalytic activity. In: *Applied Physics Letters* [on-

line]. 2016, **108**(21) [cit. 2019-05-01]. DOI: 10.1063/1.4952736. ISSN 0003-6951. Dostupné z: http://aip.scitation.org/doi/10.1063/1.4952736.

3.   PIETSCH, Ullrich, Václav HOLÝ a Tilo BAUMBACH. *High-Resolution X-Ray Scattering: From Thin Films to Lateral Nanostructures*. Second Edition. 2004. ISBN 978-144-1923-073.

Session III

SL12

THERMAL EVOLUTION AND MICROSTRUCTURE OF GAS AGGREGATION CLUSTER SOURCE PRODUCED METAL NANOPARTICLES

Tereza Kretková[1], Lukáš Horák[1], Pavel Pleskunov[2], Jan Hanuš[2], Andrei Choukourov[2], Miroslav Cieslar[3], Milan Dopita[1]

[1]Department of Condensed Matter Physics, Faculty of Mathematics and Physics, Charles University, Ke Karlovu 5, 121 16 Prague 2, Czech Republic

[2]Department of Macromolecular Physics, Faculty of Mathematics and Physics, Charles University, V Holešovičkách 2, 180 00 Prague 8, Czech Republic

[3]Department of Physics of Materials, Faculty of Mathematics and Physics, Charles University, Ke Karlovu 5, 121 16 Prague 2, Czech Republic

tkretkova@gmail.com

Nanoparticles belong to modern, progressive materials with wide application potential. Its interesting properties come from the high surface to volume ratio and often differ from the properties of bulk or coarse-grained materials with the same chemical composition. Nanoparticles catalytic, magnetic, electric or optical properties are just examples. In this study we investigated niobium nanoparticles prepared by magnetron sputtering in combination with gas aggregation cluster source operated in DC mode in argon atmosphere.

Studied nanoparticles deposited on silicon substrates were characterized by combination of X-ray scattering and diffraction methods and transmission and scanning electron microscopies with energy-dispersive X-ray spectroscopy. These analytical methods provide the information about the nanoparticles sizes, shapes, their distributions,

chemical composition and the real atomic structure. In order to determine the thermal evolution of nanoparticles microstructure, the in situ high temperature XRD measurement was done in ambient air atmosphere up to 800 C. Measured SAXS data for temperatures in range between 50 C – 800 C are shown in Figure 1. Two main transition are observed and described.

Thin oxygen layer is present on the surface of as prepared niobium nanoparticles, which acts as a protection barrier against further corrosion. The thickness of this amorphous oxide layer, as determined by fitting the SAXS patterns, is about 0.9 nm. The nanoparticle core is formed by pure niobium bcc phase and its mean radius is 11 nm. With increasing temperature, the growth of the oxide shell layer at the expense of the size of nanoparticle metallic core occurs. Slightly above 200 C the nanoparticles are fully
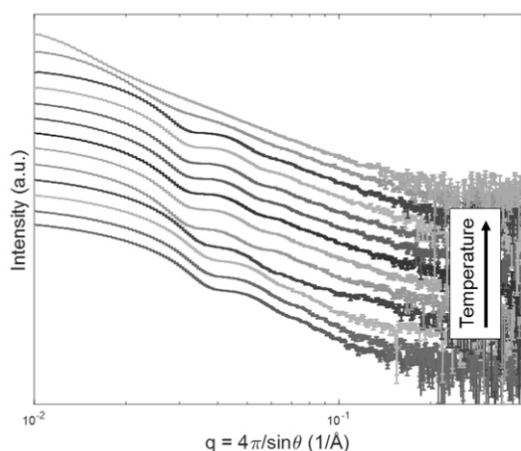
Figure 1. The SAXS patterns measured during annealing of nanoparticles from 50 °C to 750 °C, at ambient air atmosphere.
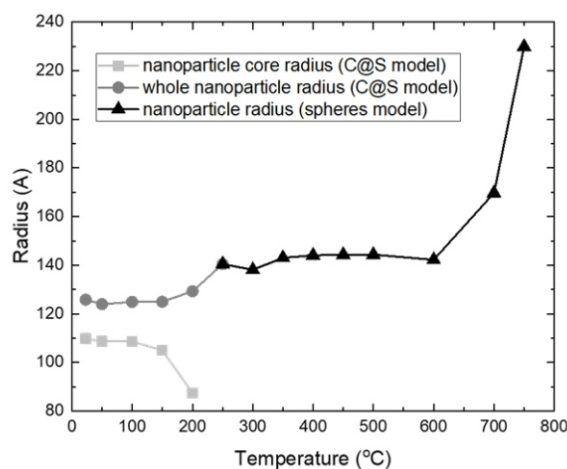
Figure 2. Temperature dependence of nanoparticle sizes, two different models were used to fit the measured data: core@shell model up to 200 °C, above 200 °C spheres model.